Experimental characterization, modeling and identification of the NEES-UCSD shake table mechanical system

O. Ozcelik[1], J. E. Luco[1,*,†], J. P. Conte[1], T. L. Trombetti[2] and J. I. Restrepo[1]

[1]*Department of Structural Engineering, University of California, San Diego, 9500 Gilman Dr, La Jolla, CA 92093-0085, U.S.A.*
[2]*Facolta di Ingegneria, Dip. D.I.S.T.A.R.T., Università degli Studi di Bologna, 40136 Bologna, Italy*

SUMMARY

This paper proposes a simple conceptual mathematical model for the mechanical components of the NEES-UCSD large high-performance outdoor shaking table and focuses on the identification of the parameters of the model by using an extensive set of experimental data. An identification approach based on the measured hysteresis response is used to determine the fundamental model parameters including the effective horizontal mass, effective horizontal stiffness of the table, and the coefficients of the classical Coulomb friction and viscous damping elements representing the various dissipative forces in the system. The effectiveness of the proposed conceptual model is verified through a comparison of analytical predictions with experimental results for various tests conducted on the system. The resulting mathematical model will be used in future studies to model the mechanical components of the shake table in a comprehensive physics-based model of the entire mechanical, hydraulic, and electronic system. Copyright © 2007 John Wiley & Sons, Ltd.

1. INTRODUCTION

1.1. Objectives of the study

Large servo-hydraulic shaking table systems are essential tools in experimental earthquake engineering. They provide effective ways to subject structural components, substructures, or entire structural systems to dynamic excitations similar to those induced by real earthquakes. In general,

---

*Correspondence to: J. E. Luco, Department of Structural Engineering, University of California, San Diego, 9500 Gilman Dr, La Jolla, CA 92093-0085, U.S.A.
†E-mail: jeluco@ucsd.edu

components of shake tables can be grouped into three sub-systems: mechanical, hydraulic, and electronic. Typically, the steel platen, vertical and lateral bearings, hold-down struts, and actuators are included in the mechanical category; pumps, accumulators, servo-valves, actuators, and surge tank are included in the hydraulic category, and finally, controller, signal conditioning units, and feedback sensors are included in the electronic category. A mathematical model of the complete shake table system is required for the planning of future experiments, for the development of safety measures, and for the optimization of the system. The first objective of this study is to develop a simplified analytical model for the mechanical sub-system of the new NEES-UCSD large high-performance outdoor shaking table (LHPOST) located at the Englekirk Structural Engineering Center at Camp Elliot Field Station. The second objective is to identify the parameters of the model using the experimental data generated during the extensive shake down tests of the NEES-UCSD LHPOST. The third objective is to validate the model and to identify parameters through detailed comparisons of analytical predictions and corresponding experimental data from tests of different types including periodic tests, white noise tests, and earthquake simulation tests. A final objective of this paper is to add to the state of the art on analytical modeling of shake table systems [1–10] by specific consideration of the large NEES-UCSD LHPOST. It is envisioned that the resulting analytical model of the mechanical sub-system will be used in future studies to comprehensively model the entire shake table system including all sub-systems mentioned above.

1.2. Overview of the NEES-UCSD LHPOST

The new NEES-UCSD LHPOST located at a site 15 km away from the main campus of the University of California at San Diego (32°53′37″N and 117°06′32″W) is a unique outdoor experimental facility that enables next-generation seismic tests to be conducted on very large structural and

Figure 1. NEES-UCSD LHPOST with a full-scale 21 m high wind turbine mounted on it.
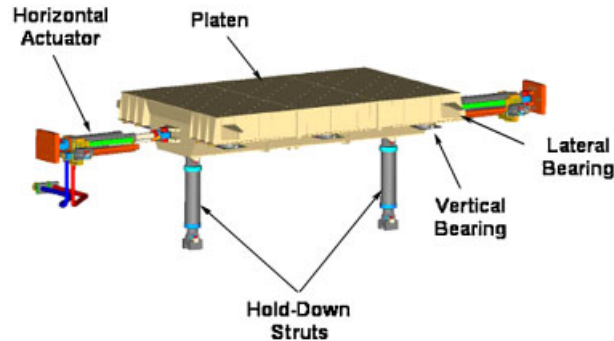
Figure 2. Mechanical sub-system of NEES-UCSD LHPOST.

soil–foundation–structure interaction systems (Figure 1). The LHPOST consists of a moving steel platen (7.6 m wide by 12.2 m long); a reinforced concrete reaction block; two servo-controlled dynamic actuators with a force capacity in tension/compression of 2.6 and 4.2 MN, respectively; a platen sliding system (six pressure-balanced vertical bearings with a force capacity of 9.4 MN each and a stroke of ±0.013 m); an overturning moment restraint system (a pre-stressing system consisting of two nitrogen-filled hold-down struts with a stroke of 2 m and a hold-down force capacity of 3.1 MN each); a yaw restraint system (two pairs of slaved pressure balanced bearings along the length of the platen); a real-time multi-variable controller, and a hydraulic power supply system. A three-dimensional rendering of the mechanical components is presented in Figure 2.

The technical specifications of the LHPOST include a stroke of ±0.75 m, a peak horizontal velocity of 1.8 m/s, a peak horizontal acceleration of $4.2g$ for bare table conditions and $1.0g$ for a rigid payload of 400 ton, a horizontal force capacity of 6.8 MN, an overturning moment capacity of 50 MN m, and a vertical payload capacity of 20 MN. The frequency bandwidth is 0–20 Hz. Other detailed specifications of the NEES-UCSD LHPOST can be found elsewhere [11, 12].

1.3. Model formulation and identification approach

The large lateral displacement of the platen of ±0.75 m and the resulting rotation and elongation of the hold-down struts raise the possibility of non-negligible nonlinear terms in the equations of motion of the mechanical system. As a first task, the equations of motion including nonlinear terms are derived using a Lagrangian approach, and the order of magnitude of the nonlinear terms is estimated. On the basis of the known physical properties of the system and of the operational limits of the shake table, it is shown that the contributions of the nonlinear terms are small and that a simplified model with a mass, horizontal stiffness, and a dissipative mechanism composed of Coulomb friction and viscous resisting forces is sufficient to capture the salient characteristics of the mechanical sub-system of the LHPOST. Even though more complex models are available in the literature for modeling friction and viscous forces [13], classical discontinuous Coulomb friction and viscous damping models are adopted in this initial study.

The characteristics of the mechanical system are obtained by analysis of the hysteresis loops relating the total feedback actuator force with the feedback displacement, velocity and acceleration of the platen recorded during periodic tests. The procedure takes advantage of the periodicity of the table motion to isolate the inertial, elastic and dissipative forces and their respective dependence on acceleration, displacement and velocity. The approach is restricted to periodic tests, but does not assume *a priori* a linear model. Other complementary identification approaches will be presented elsewhere.

1.4. Shakedown test program

A large shakedown test program was performed on the LHPOST system to verify compliance with the design specifications, and also to identify the fundamental characteristics of the NEES-UCSD shake table. The tests included periodic, earthquake, and white noise tests. Twelve sinusoidal (S) and twelve triangular (T) tests with rounded waveforms were used with amplitude and frequency characteristics spanning the operational frequency range of the system (Tables I and II). For the earthquake tests, full and scaled versions of historical earthquake records with different characteristics were used. Finally, several white noise tests with different root-mean-square accelerations were performed.

The periodic tests were performed with forces of 0, 1042 and 2085 kN in each of the two hold-down struts. These forces correspond to internal pressures in the hold down struts of 0, 6.9 and 13.8 MPa, respectively. These tests were aimed at determining the effective horizontal stiffness associated with the hold-down struts and also to investigate the effect of vertical loads on the dissipative (friction, damping) forces. All other tests were performed with the operational force of 2085 kN (13.8 MPa nitrogen pressure) in each of the two hold-down struts. All tests were repeated at least two times to check for repeatability.

Table I. Estimates of the effective horizontal stiffness K_e from triangular tests (13.8 MPa hold-down nitrogen pressure).

Test	T1	T2	T3	T5	T7	T9	T4	T6	T10	T12	T8	T11
Frequency (Hz)	0.05	0.05	0.05	0.10	0.10	0.40	0.05	0.10	0.40	0.67	0.17	0.50
u_{max} (cm)	5	7.50	12.50	25	37.50	46.88	50	62.50	62.50	67.50	75	75
$\dot{u}_{max}$ (cm/s)	1	1.50	2.50	10	25	75	10	25	100	180	50	150
K_e (MN/m)	1.25	1.27	1.27	1.25	1.27	1.25	1.27	1.27	1.25	1.24	1.27	1.25

Table II. Estimates of effective horizontal longitudinal mass M_e from sinusoidal tests (13.8 MPa hold-down nitrogen pressure).

Test	S4	S6	S5	S7	S9	S10	S8	S11	S12
Frequency (Hz)	0.40	0.40	1.00	0.80	0.60	0.80	1.20	1.20	1.43
u_{max} (cm)	4	10	4	10	20	20	10	20	20
$\dot{u}_{max}$ (cm/s)	10.05	25.12	25.12	50.24	75.36	100.48	75.36	150.72	179.61
$\ddot{u}_{max}$ (g)	0.026	0.064	0.161	0.257	0.29	0.515	0.579	1.158	1.644
M_e (ton)	150	158	144	144	144	144	144	144	120

1.5. Sensors and data acquisition system

Data were acquired by the same built-in sensors and data acquisition (DAQ) system used to control the shake table. The DAQ system has low-pass anti-aliasing filtering capabilities and a default sampling rate of 1024 Hz. The displacement of the platen relative to the reaction block was measured by two digital displacement transducers (Temposonics® linear transducers) located on the East and West actuators. The platen acceleration response was measured by two Setra®-Model 141A accelerometers with a range of $\pm 8g$ and a flat frequency response from DC to 300 Hz. However, the signal conditioners used for the accelerometers included a built-in analog low-pass filter with cut-off frequency set at 100 Hz. Pressure in the actuator chambers was measured by four Precise Sensors®-Model 782 pressure transducers with a pressure range from 0 to 68.9 MPa and a (sensor/DAQ) resolution of 689.5 Pa. These pressure transducers are located near the end caps of each actuator. Measured pressures are converted to actuator forces by multiplying them by the corresponding actuator piston areas and combining the contributions from both chambers. The pressure recordings were high-pass filtered to remove static pressure components, but were not low-pass filtered. The velocity of the platen is not measured directly but is estimated by using a crossover filter that combines the differentiated displacement with the integrated acceleration [14]. The MTS 469D Seismic Controller Recorder software was used to record the digitized data. The sampling rate of the recorder was set at 512 Hz during the tests, and the built-in anti-aliasing digital filter was enabled during the tests.

In all the tests performed, two apparent harmonic signals at 10.66 and 246 Hz were observed in records of the total actuator force and, to a lesser degree, on table acceleration records. The signal at 10.66 Hz corresponds to the oil column frequency of the system [4, 10, 15] which is excited when there is a sudden change in the motion of the platen. The most likely source of the second harmonic signal at 246 Hz is the resonance between the pilot stage and the third stage of the servo-valves. Due to low-pass filtering of the acceleration records at 100 Hz, this 246 Hz harmonic signal can be observed only slightly in the acceleration records.

2. ANALYTICAL MODEL OF THE MECHANICAL SUB-SYSTEM OF THE SHAKE TABLE

The forces exerted on the platen by the horizontal actuators are balanced by: (1) the inertia force due the mass of the platen, hold-down struts and moving parts of the actuators; (2) the elastic restoring force due to the nitrogen pressure inside the inclined hold-down struts; (3) the Coulomb-type dissipative forces due to (i) sliding of the platen (wear plates) on the vertical and lateral bearings, (ii) rotation of hinges (swivels) at both ends of the hold-down struts, and (iii) sliding of the actuator arm and piston inside each of the two horizontal actuators; and finally (4) the viscous-type dissipative forces due to various sources, such as (i) oil film between the wear plates and the vertical and lateral bearings, (ii) air flow in and out of the hold-down struts, and (iii) cross-port leakage in the horizontal actuators, which accounts for the damping within the actuators [16].

It is important to note that the mechanical sub-system considered here does not include the compressible oil columns in the actuator chambers. The recorded actuator forces obtained from the pressures on both sides of the pistons already account for the oil column effect. However, some contamination with the oil column arises because the pressure transducers are located at the end caps of the actuators and not directly on the pistons.

As a first approximation, the platen is treated here as a rigid body of mass M_{pl} which undergoes a total translation u_x along the longitudinal x-axis. The six vertical bearings and the four lateral bearings are modeled as dissipative elements including Coulomb friction and viscous damping. The hold-down struts contribute to the inertial, elastic, and dissipative forces on the system. The equation of motion for the mechanical sub-system of the NEES-UCSD LHPOST can be written as

$$F_I(t) + F_E(t) + F_D(t) = F_A(t) \tag{1}$$

where $F_A(t)$ is the resultant horizontal longitudinal force from both actuators, and F_I, F_E, and F_D are the inertia, elastic, and damping forces, respectively. These forces can be expressed as

$$F_I = M_e \ddot{u}_x + 2\overline{M}'_e \left(\frac{u_x}{h}\right)^2 \ddot{u}_x + 2\overline{M}'_e \left(\frac{\dot{u}_x}{h}\right)^2 u_x \tag{2}$$

$$F_E = K_e u_x + K'_e \left(\frac{u_x}{h}\right)^2 u_x \tag{3}$$

$$F_D = \left[F_\mu + C_e |\dot{u}_x|^\alpha + 2c_\beta \left| \frac{u_x}{h} \right|^{1+\beta} |\dot{u}_x|^\beta + \mu_e^{(iv)} F_{hd} \left(\frac{u_x}{h} \right)^2 \right] \text{sign}(\dot{u}_x) \tag{4}$$

where the meaning of the various terms is given below.

Effective masses: The effective mass terms appearing in Equation (2) are given approximately by

$$M_e = M_{pl} + 2M_{act} + 2\overline{M}_e \tag{5a}$$

$$\overline{M}_e = \frac{1}{3} M_1 \left(\frac{l_0}{h}\right)^2 + \frac{1}{3} M_2 \tag{5b}$$

$$\overline{M}'_e = \frac{1}{2} \left[\frac{5}{3} M_2 - \frac{4}{3} M_1 \left(\frac{l_0}{h}\right)^2 \right] \tag{5c}$$

where M_{pl} is the mass of the platen; M_{act} is the mass of the moving parts of a single actuator; M_1 and M_2 are the masses of the piston and cylinder of one hold-down strut, respectively; and l_0 and h are the corresponding lengths.

The second term in Equation (2) amounts to less than 0.05% of the first term, and can be ignored. The last term in Equation (2) corresponds to a force of less than 0.25 kN which is also negligible. Thus, only the first term in Equation (2) is significant. Finally, the combined effective mass $2\overline{M}_e$ of the hold-down struts is of the order of 3% of the mass M_{pl} of the platen.

Effective horizontal stiffness due to Hold-Down struts: Assuming adiabatic conditions, the effective stiffness terms appearing in Equation (3) can be obtained from

$$K_e = \frac{2p_0 A}{h} \tag{6a}$$

$$K'_e = \frac{1}{2} \left(\frac{\gamma h}{l_0} - 1 \right) K_e \tag{6b}$$

where p_0 is the initial pressure inside the nitrogen-filled chamber of a hold-down strut, A is the cross-section area of the strut cylinder, h is the (fixed) height from pin-to-pin of the hold-down strut in its initial configuration ($u_x = 0$), l_0 is the initial length of the piston, and γ is the gas

constant (i.e. the ratio of the heat capacity at constant pressure to that at constant volume). For the hold-down struts of the UCSD-NEES Table, $h = 3.3$ m, $l_0 = 2.1$ m, $\gamma = 1.44$ and $u_x \leqslant 0.75$ m. In this case, the ratio $\overline{K}'_e (u_x/h)^2 / \overline{K}_e$ amounts to less than 3.3%. Therefore, the relative contribution of the nonlinear elastic restoring force term is small and can be neglected in most cases. However, for large displacements ($u_x \approx 0.75$ m), the elastic force associated with the nonlinear term can reach a value of about 30 kN which is comparable to some of the components of the dissipative force.

Effective lateral dissipative forces: Finally, the first term in Equation (4) corresponds to the Coulomb frictional force given by

$$F_\mu = \mu'_e F_{hd} + \mu''_e F_{pl+act} + \mu'''_e F_l \tag{7a}$$

$$\mu'_e = \mu''_e + 2\mu_{hg}\kappa \left(\frac{a}{h}\right) \tag{7b}$$

where $F_{hd} = 2p_0 A$ is the initial vertical force due to pre-charge nitrogen pressure in the hold-down struts, F_{pl+act} is the combined weight of the platen and part of the actuators supported by the vertical bearings; F_l is the time dependent total normal force on the lateral bearings; μ''_e and μ'''_e are the Coulomb friction coefficients on the vertical and lateral bearings, respectively; μ_{hg} is the Coulomb friction coefficient in the swivels of the hold-down struts; a is the radius of the hinge and κ is a constant that depends on the distribution of forces on the hinge. The second term in Equation (4) represents viscous damping in the actuators in which C_e is an effective viscous damping constant and $0 \leqslant \alpha \leqslant 1$. The third term in Equation (4) represents viscous damping in the hold-down struts with $0 \leqslant \beta \leqslant 1$. Finally, the last term in Equation (4) is a nonlinear term involving friction on the hinges of the hold-down struts. In that term

$$\mu_e^{(iv)} = 2\mu_{hg}\kappa \left(\frac{a}{h}\right) \frac{\gamma}{2} \left(\frac{h}{l_0}\right) \tag{8}$$

It will be shown later that the first two terms in Equation (4) are sufficient to account for most of the dissipative forces.

3. PARAMETER ESTIMATION BY ANALYSIS OF HYSTERESIS LOOPS

In this section, the hysteresis loops relating actuator force to displacement, velocity, or acceleration of the table during periodic triangular or sinusoidal tests will be used to determine the most important characteristics of the shake table mechanical system. The basic conceptual model of the system, inspired in part by Equations (1)–(4), is expressed by

$$M_e(u_x)\ddot{u}_x(t) + F_E(u_x) + F_D(\dot{u}_x) = F_A(t) \tag{9}$$

where $u_x(t)$ is the horizontal longitudinal total displacement of the platen, M_e is the effective mass, and F_E, F_D, and F_A are the total elastic, dissipative, and actuator forces, respectively. It is assumed that $M_e(u_x)$ is an even function of u_x, and that $F_E(u_x)$ and $F_D(\dot{u}_x)$ are odd functions of u_x and $\dot{u}_x$, respectively. The simplified model given by Equation (9) excludes dependence of F_E and F_D on the history of u_x and $\dot{u}_x$, and ignores certain possible inertial and dissipative terms that depend on products of u_x and $\dot{u}_x$.

The data from periodic tests were low-pass filtered, except where noted, with a cut-off frequency of four times the fundamental frequency of the test in an attempt to keep the first few harmonics of the potentially nonlinear response while filtering out higher frequencies. To ensure that the steady-state response had been reached, the analysis of the response was based on the second to the last cycle of each test. Finally, in the case of the triangular tests, only the portions of the time histories over which constant velocities had been reached were used in the identification procedure.

The identification approach used here takes advantage of the periodic nature of $u_x(t)$, $\dot{u}_x(t)$, and $\ddot{u}_x(t)$ during a test cycle ($0 < t < T$). Selecting the cycle of test data so that the displacement $u_x(t)$ is positive over the first half ($0 < t < T/2$) of the cycle; the following time instants t_1, t_2, t_3, and t_4 are considered: $0 < t_1 < T/4$, $t_2 = T/2 - t_1$, $t_3 = T/2 + t_1$, and $t_4 = T - t_1$. With this notation, the periodicity leads to

$$u_x(t_2) = u_x(t_1), \quad \dot{u}_x(t_2) = -\dot{u}_x(t_1), \quad \ddot{u}_x(t_2) = \ddot{u}_x(t_1) \tag{10a}$$

$$u_x(t_4) = u_x(t_3), \quad \dot{u}_x(t_4) = -\dot{u}_x(t_3), \quad \ddot{u}_x(t_4) = \ddot{u}_x(t_3) \tag{10b}$$

and

$$u_x(t_4) = -u_x(t_1), \quad \dot{u}_x(t_4) = \dot{u}_x(t_1), \quad \ddot{u}_x(t_4) = -\ddot{u}_x(t_1) \tag{11a}$$

$$u_x(t_3) = -u_x(t_2), \quad \dot{u}_x(t_3) = \dot{u}_x(t_2), \quad \ddot{u}_x(t_3) = -\ddot{u}_x(t_2) \tag{11b}$$

Applying Equation (9) at times t_1 and t_2, t_3 and t_4, t_1 and t_4, and t_2 and t_3 leads to

$$M_e(u_x(t_1))\ddot{u}_x(t_1) + F_E(u_x(t_1)) = [F_A(t_1) + F_A(t_2)]/2 \tag{12}$$

$$M_e(u_x(t_3))\ddot{u}_x(t_3) + F_E(u_x(t_3)) = [F_A(t_3) + F_A(t_4)]/2 \tag{13}$$

$$F_D(\dot{u}_x(t_1)) = [F_A(t_1) + F_A(t_4)]/2 \tag{14}$$

$$F_D(\dot{u}_x(t_2)) = [F_A(t_2) + F_A(t_3)]/2 \tag{15}$$

Equations (14) and (15) indicate that the dissipative forces can be obtained directly from the data. On the other hand, Equations (12) and (13) indicate that additional considerations need to be made to separate the inertial and elastic forces.

3.1. Estimation of elastic forces and effective horizontal stiffness

To separate the elastic forces from the inertial and dissipative forces, the results of the periodic triangular tests, in which the horizontal acceleration $\ddot{u}_x$ of the platen is zero for intervals of time are used. In this case, Equations (12) and (13) reduce to

$$\begin{aligned} F_E(\overline{u}_x(t)) &= \tfrac{1}{2}[F_A(t) + F_A(T/2 - t)] \\ \overline{u}_x(t) &= \tfrac{1}{2}[u_x(t) + u_x(T/2 - t)] \quad (0 < t < T/4) \end{aligned} \tag{16}$$

and

$$\begin{aligned} F_E(\overline{u}_x(t)) &= \tfrac{1}{2}[F_A(t) + F_A(3T/2 - t)] \\ \overline{u}_x(t) &= \tfrac{1}{2}[u_x(t) + u_x(3T/2 - t)] \quad (T/2 < t < 3T/4) \end{aligned} \tag{17}$$

which provide estimates of $F_E(\overline{u}_x)$ for $\overline{u}_x > 0$ and $\overline{u}_x < 0$, respectively.
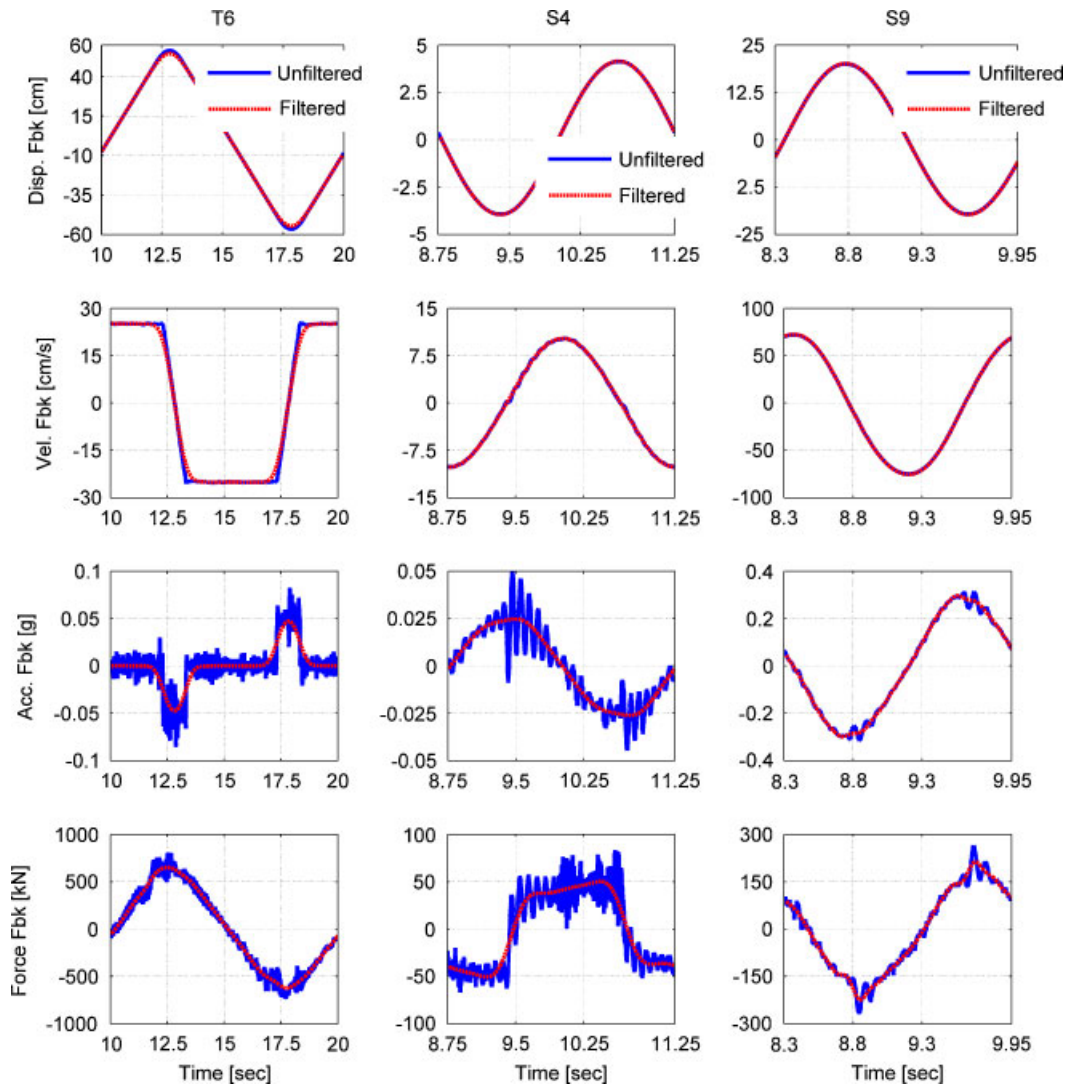
Figure 3. Filtered and unfiltered time history plots of tests T6, S4, and S9.

The typical basic data for the procedure are illustrated in Figure 3 (left) which shows time histories of the recorded platen displacement, velocity and acceleration, and of the actuator force $F_A(t)$ for one cycle of test $T6(u_{max} = 62.5\,cm, \dot{u}_{max} = 25.0\,cm/s, T = 10\,s)$. The plots show the original unfiltered data as well as the filtered data after use of a low-pass filter with a cut-off frequency of 0.4 Hz. The unfiltered actuator force data contain harmonic components at the oil-column frequency of 10.66 Hz and at 246 Hz. It is apparent from Figure 3 (left) that over portions of the cycle the displacement varies linearly with time, and that the acceleration is practically zero during these intervals.
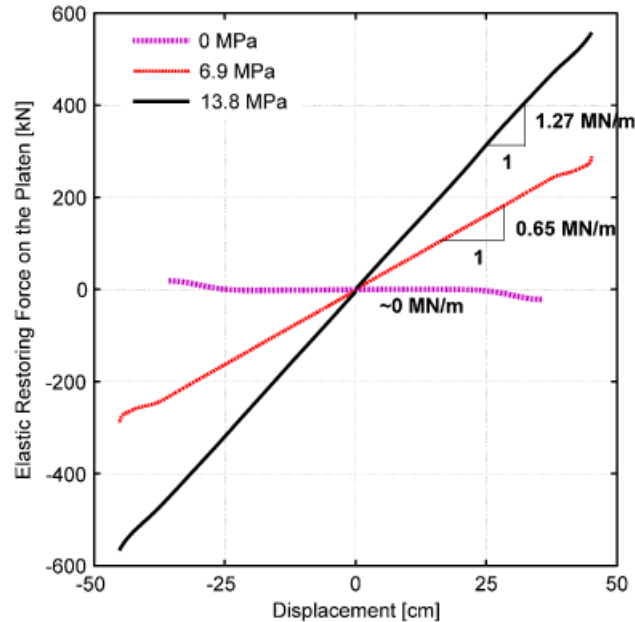
Figure 4. Estimates of the horizontal stiffness by hysteresis loop approach from triangular test T4 for 0, 6.9 and 13.8 MPa nitrogen pressure in the hold-down struts.

The relation between F_E and u_x can be obtained from Equations (16) and (17) by using the time t as an internal variable relating $F(u_x(t))$ and $u_x(t)$. As an illustration, the results obtained for test T4($u_{max} = 50$ cm, $\dot{u}_{max} = 10$ cm/s, $T = 20$ s) for pressures of 0, 6.9, and 13.8 MPa in the hold-down struts are shown in Figure 4. It is apparent from Figure 4 that the total elastic restoring force depends linearly on the platen displacement, that the elastic force is essentially zero when the hold-down force is zero, and that the elastic force for a hold-down pressure of 6.9 MPa is half of that for the operational hold-down pressure of 13.8 MPa.

The results in Figure 4 as well as similar results for other triangular tests indicate that the elastic restoring force acting on the platen is essentially provided by the nitrogen pre-charge pressure in the hold-down struts. The effective horizontal stiffness values obtained from the slopes of the lines in Figure 4 correspond to $K_e = 1.27$ MN/m for the operational pressure of 13.8 MPa, and $K_e = 0.65$ MN/m for a pressure of 6.9 MPa. The estimates of the stiffness K_e at the operational pressure (13.8 MPa) obtained from all triangular tests are listed in Table I. The estimates in Table I decreases slightly for tests involving velocities above 50 cm/s (T9–T11). Since the triangular pulses are severely distorted at high velocities, the average stiffness $K_e = 1.266$ MN/m from tests T1–T8 will be taken as the representative value for the effective stiffness. The experimentally obtained stiffness $K_e = 1.266$ MN/m agrees almost exactly with the theoretical combined stiffness $K_e = 2Ap_0/h$ of the two hold-down struts which takes the value $K_e = 1.26$ MN/m for $A = 0.15$ m^2 (effective cross-section area of nitrogen chamber in each strut), $p_0 = 13.8$ MPa (internal pressure), and $h = 3.3$ m (length of the hold-down struts).

Finally, the theoretical equations of motion presented in Section 2 indicate that the total non-dissipative force for $\ddot{u}_x = 0$ can be expressed by $K_e u_x + K_e'(u_x/h)^2 u_x + 2\overline{M}_e'(\dot{u}_x/h)^2 u_x$ where

K_e, K'_e, and $\overline{M}'_e$ are given by Equations (5a)–(5c) and (6a) and (6b). The linear nature of the experimentally determined elastic force F_E confirms that the second (cubic) term is negligible compared with the first term. The last term $2\overline{M}'_e(\dot{u}_x/h)^2 u_x$ is an inertial term associated with the rotation of the hold-down struts. For triangular tests in which $\dot{u}_x^2$ is constant, this term can be confounded with the first term $K_e u_x$ as both are proportional to u_x. The results in Figure 4 for tests with different velocities, as well as the vanishing stiffness obtained for zero hold-down pressure confirm that the effect of this inertia term is negligible.

3.2. Estimation of effective mass

Having established that $F_E(u_x) = K_e u_x$ where $K_e = 1.266\,\text{MN/m}$ (for $p_0 = 13.8\,\text{MPa}$), Equations (12) and (13) can be used to obtain estimates of the effective mass $M_e(u_x)$ in the form

$$M_e(\overline{u}_x(t))\ddot{\overline{u}}_x(t) = \tfrac{1}{2}[F_A(t) - K_e u_x(t)] + \tfrac{1}{2}[F_A(T/2 - t) - K_e u_x(T/2 - t)] \quad (18a)$$

$$\ddot{\overline{u}}_x(t) = \tfrac{1}{2}[\ddot{u}_x(t) + \ddot{u}_x(T/2 - t)] \quad (0 < t < T/4) \quad (18b)$$

for $\ddot{\overline{u}}_x > 0$, and

$$M_e(\overline{u}_x(t))\ddot{\overline{u}}(t) = \tfrac{1}{2}[F_A(t) - K_e u_x(t)] + \tfrac{1}{2}[F_A(3T/2 - t) - K_e u_x(3T/2 - t)] \quad (19a)$$

$$\ddot{\overline{u}}_x(t) = \tfrac{1}{2}[\ddot{\overline{u}}_x(t) + \ddot{\overline{u}}_x(3T/2 - t)] \quad (T/2 < t < 3T/4) \quad (19b)$$

for $\ddot{\overline{u}}_x < 0$.

Since during triangular tests, the acceleration spikes at the time of change in velocity and is nearly zero at any other times, sinusoidal tests are preferred to determine the effective horizontal mass. The typical data including $u_x(t)$, $\dot{u}_x(t)$, $\ddot{u}_x(t)$, and $F_A(t)$ are illustrated in Figure 3 (right) for one cycle of the sinusoidal test S9 ($u_{max} = 20\,\text{cm}$, $\dot{u}_{max} = 75.4\,\text{cm/s}$, $\ddot{u}_{max} = 0.29g$, $T = 1.67\,\text{s}$) performed under the operational hold-down pressure of 13.8 MPa. The original data and the data after a low-pass filter with cut-off frequency of 2.4 Hz had been applied are superimposed in Figure 3 (right). The unfiltered data include components at the oil-column frequency of 10.66 Hz which are excited every time the velocity of the table changes sign.

The relation between the inertia force $M_e(u_x)\ddot{u}_x$ and the acceleration $\ddot{u}_x$ for sine tests S9 ($\ddot{u}_{max} = 0.29g$) and S10 ($\ddot{u}_{max} = 0.51g$) is shown in Figure 5 for the operational hold-down pressure of 13.8 MPa. The results obtained indicate that the inertial force for the sinusoidal tests is essentially a linear function of the acceleration $\ddot{u}_x$, and consequently, that the effective mass M_e is a constant. The slope of the curves in Figure 5 indicate that $M_e = 144\,\text{ton}$. The results for other sinusoidal tests with peak accelerations in the range between $0.1g$ and $1.2g$ are similar as shown in Table II. For tests (S1, S2, S3) involving extremely small accelerations ($<0.2\%g$), the inertial forces are extremely small and the results obtained are not reliable. For test S12 involving large velocities (180 cm/s) and accelerations ($1.6g$) the sinusoidal pulses are distorted and the results for M_e are not reliable.

The estimate of the effective horizontal longitudinal mass ($M_e = 144\,\text{ton}$) can be compared with the mass of the platen estimated from drawings to be about 134.8 ton. Also, data recorded on the six vertical pressure balance bearings when the hold-down struts were not pressurized indicate a total weight of 1.613 MN including the weight of the platen and of the cylinders of the two hold-down struts, and part of the weights of the two actuators. The corresponding total mass is 164.5 ton. The effective lateral mass should be smaller than the total vertical mass obtained from
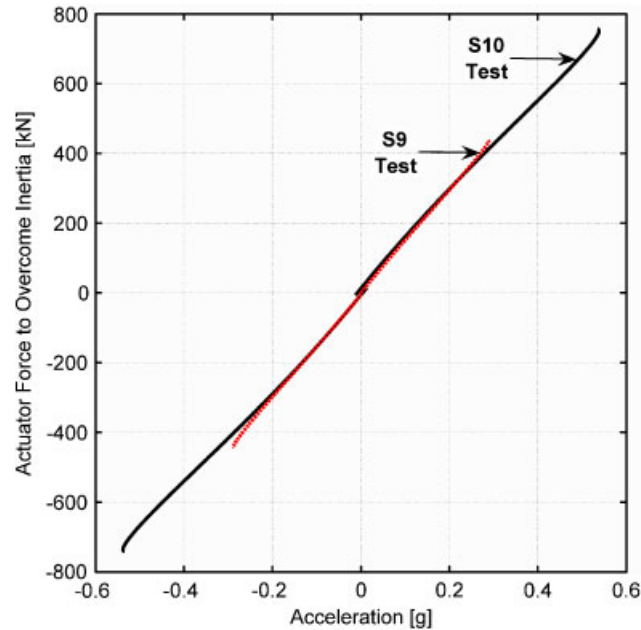
Figure 5. Estimates of effective mass obtained by hysteresis loop approach from sinusoidal tests S9 and S10 for 13.8 MPa nitrogen pressure in the hold-down struts.

the vertical bearings because only the mass of the pistons of the actuators and a fraction of the mass of the hold-down struts affect the lateral mass. Also, the flexibility of the platen, albeit small, would result in a smaller effective mass.

3.3. Estimation of the effective total dissipative forces

Equations (14) and (15) are used here to separate the total dissipative forces from the inertial and elastic components of the total actuator force. In particular, the dependence of the total dissipative forces on velocity is given by

$$F_D(\bar{\dot{u}}_x(t)) = [F_A(t) + F_A(T - t)]/2 \tag{20a}$$

$$\bar{\dot{u}}(t) = [\dot{u}_x(t) + \dot{u}_x(T - t)]/2 \tag{20b}$$

with $0 < t < T/4$ for $\dot{u}_x > 0$, and $T/4 < t < T/2$ for $\dot{u}_x < 0$.

The typical data required to apply the proposed identification procedure are illustrated in Figure 3 (center) which includes one cycle of the filtered and unfiltered time history plots of the platen response and the total actuator force obtained during test S4 ($\dot{u}_{max} = 10$ cm/s, $T = 2.5$ s). The unfiltered time history of the total actuator force shows that the signal is contaminated by high-frequency noise and by two harmonic signals at 10.66 and 246 Hz. A close examination of the velocity and the total actuator force time histories reveals that a jump in the total actuator force occurs whenever the platen changes the direction of motion (i.e. velocity changes the sign). To preserve this jump while removing other spurious signals, an FIR filter of order 512 with a cut-off
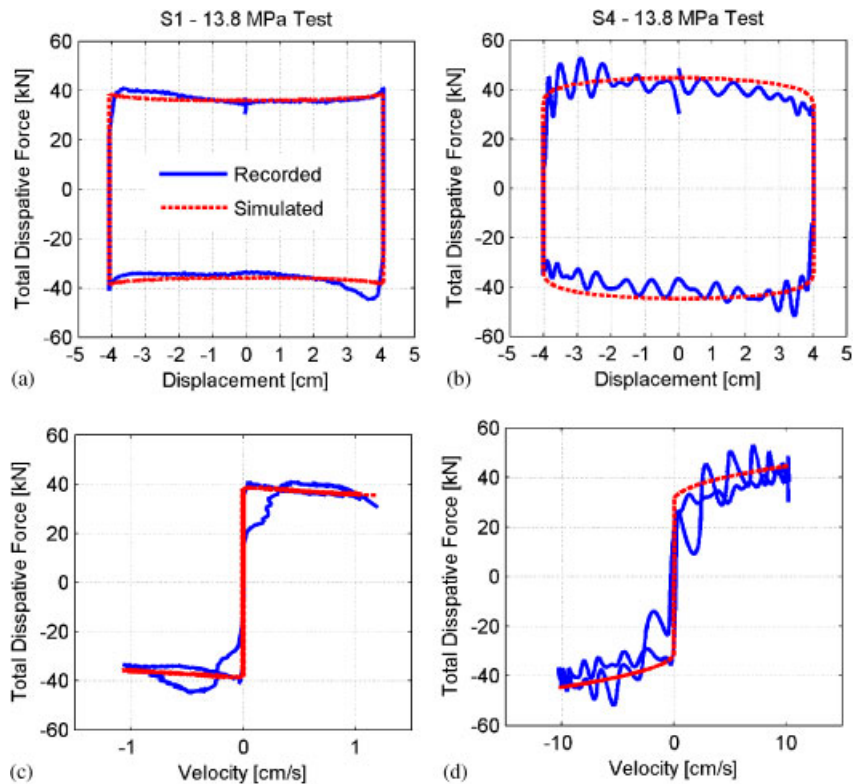
Figure 6. Comparison of recorded and simulated total dissipative forces *vs* table displacement (a, b) and velocity (c, d) for tests S1 and S4 (13.8 MPa nitrogen pressure in hold-down struts).

frequency of 8 Hz was used for all tests. This cut-off frequency is well above the frequencies of the tests, but is below the oil-column frequency. The filtered time history in Figure 3 (center) shows that the jump in the total actuator force is preserved, while the high-frequency components of this signal are filtered out.

Figure 6 illustrates the relationship between the total dissipative force and platen displacement (a, b) as well as the relationship between the total dissipative force and platen velocity (c, d) for sinusoidal tests S1 ($\dot{u}_{max} = 1.0$ cm/s), and S4 ($\dot{u}_{max} = 10$ cm/s). It is apparent from the results in Figure 6 and from additional results for tests S2 ($\dot{u}_{max} = 1.5$ cm/s), and S3 ($\dot{u}_{max} = 2.5$ cm/s) that the total dissipative force, after reaching a peak of 35–45 kN at very low velocities, decreases slightly to 30–35 kN at a velocity of 1–2 cm/s, and then increases again to about 40 kN for a velocity of 10 cm/s. The initial drop may be associated with a change of the Coulomb friction coefficient from its static value to its dynamic value. The increment of the total dissipative force at higher velocities probably reflects viscous-type dissipative forces which do not appear to increase linearly with velocity. Finally, the slightly different behavior at low velocities for the different tests suggests that the dissipative force is not only a function of the instantaneous velocity, but also of some other characteristics of the time history of motion.
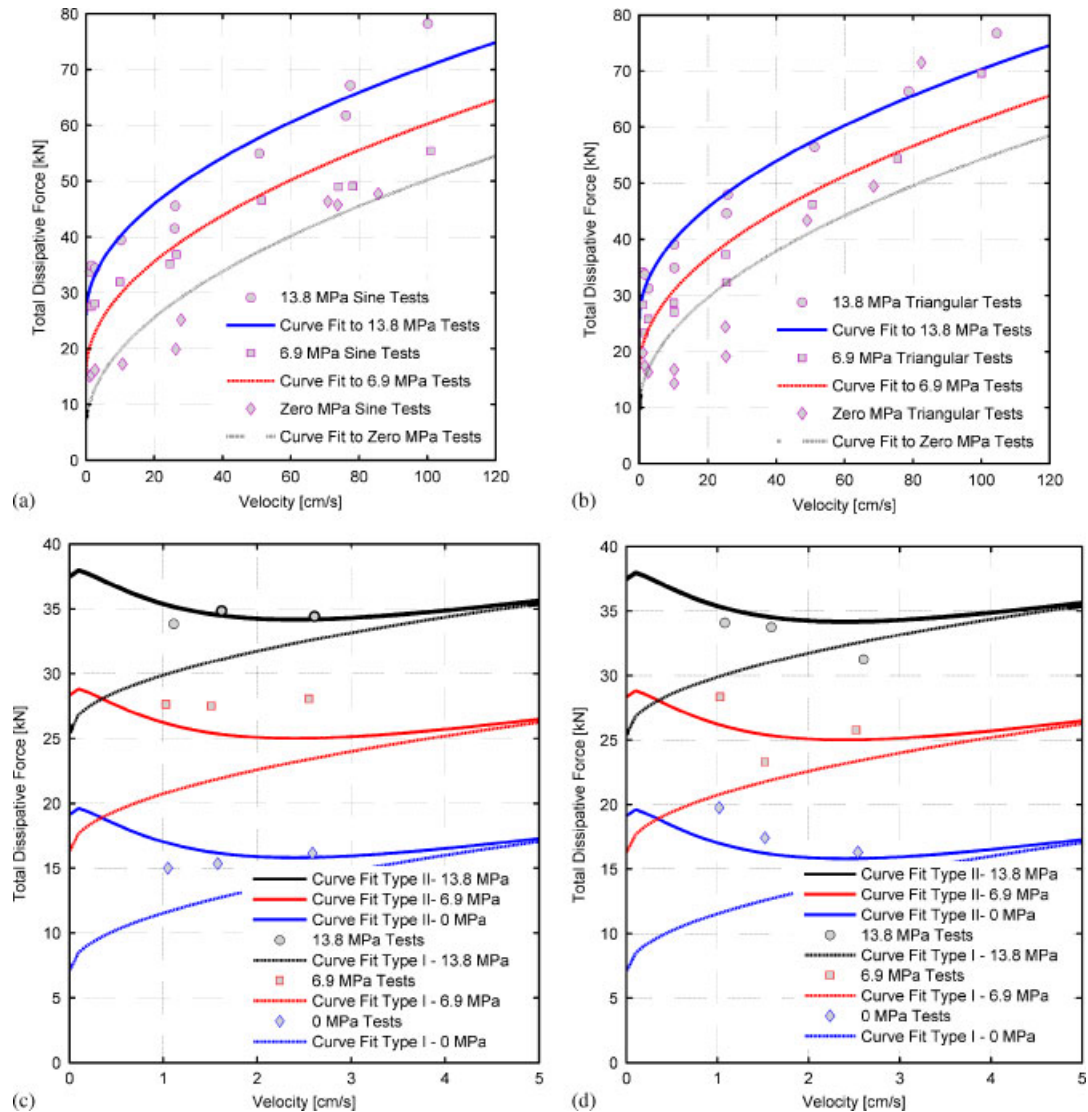
Figure 7. Total dissipative forces at maximum obtained velocities during (a) sinusoidal, and (b) triangular tests performed under 0.0, 6.9, and 13.8 MPa nitrogen pressures in the hold-down struts, and total dissipative forces observed during (c) the sinusoidal, and (d) triangular low velocity tests. Curves labeled I and II correspond to Equations (22) and (21), respectively.

The variation of the total dissipative force at higher velocities can be studied by considering the total dissipative forces obtained at the maximum achieved platen velocities in each of the sinusoidal and triangular tests performed under 13.8, 6.9 and 0.0 MPa nitrogen pressures in the hold-down struts. The results shown as individual points in Figure 7 indicate that the total dissipative force increases with both hold-down pressure and some fractional power of velocity. After some

numerical experimentation, it was decided to consider a model of the type

$$F_{\mathrm{D}}(t) = F_{\mu_{\mathrm{e}}} + C_{\mathrm{e}}|\dot{u}_x(t)|^{0.5} \tag{21}$$

in which $F_{\mu_{\mathrm{e}}}$ denotes a Coulomb friction force, while C_{e} is a fractional-power viscous damping coefficient. When this model was applied to the sinusoidal tests for the nominal hold-down pressure of 13.8 MPa, best-fit values of $F_{\mu_{\mathrm{e}}} = 26.00$ kN and $C_{\mathrm{e}} = 44.58$ kN/(m/s)$^{1/2}$ were obtained. The parameter C_{e} was then kept fixed at 44.58 kN/(m/s)$^{1/2}$ and the best fit values of $F_{\mu_{\mathrm{e}}}$ for the six groups of tests shown in Figure 7 were obtained. The resulting values of $F_{\mu_{\mathrm{e}}}$ for sinusoidal tests with hold-down pressures of 0.0, 6.9, and 13.8 MPa are 5.63, 15.65 and 26.00 kN, respectively. The corresponding values of $F_{\mu_{\mathrm{e}}}$ for the triangular tests are 9.69, 16.75 and 25.74 kN, respectively. Clearly, the parameters obtained for the sinusoidal and triangular tests are in reasonable agreement for hold-down pressures of 6.9 and 13.8 MPa. The comparisons of the model and data shown in Figure 7 also show a reasonable agreement for these pressures but not for the case of zero pressure.

3.4. Decomposition of the total dissipative force

To further study the nature of the dissipative forces, the average of the values of the terms $F_{\mu_{\mathrm{e}}}$ obtained from sinusoidal and triangular tests are plotted in Figure 8 *vs* the total vertical force F_z acting on the vertical bearings for the three different hold-down pressures considered. The average values of $F_{\mu_{\mathrm{e}}}$ for hold-down nitrogen pressures of 0.0, 6.9, and 13.8 MPa are 7.66, 16.20, and 25.87 kN, respectively. The corresponding resultant vertical forces F_z based on pressure readings
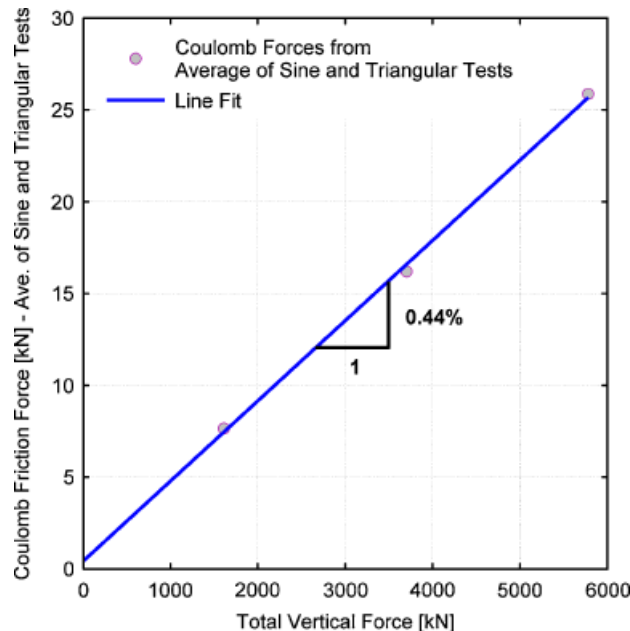
Figure 8. Coulomb friction force obtained from average of sinusoidal and triangular test results as a function of total vertical force.
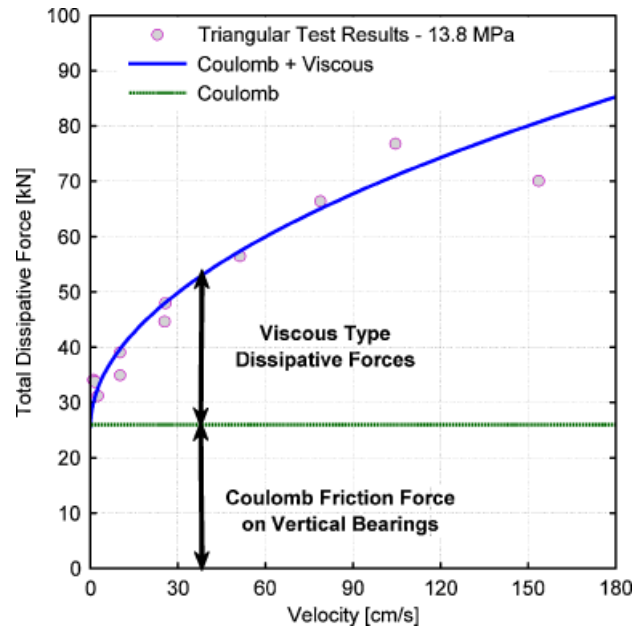
Figure 9. Decomposition of the total dissipative force into its major components.

on the six vertical bearings are 1.613, 3.698, and 5.783 MN, respectively. The results in Figure 8 indicate that there is a linear relation between F_{μ_e} and F_z, i.e. $F_{\mu_e} = \mu_e F_z$, implying that the term F_{μ_e} does represent a Coulomb friction force acting on the vertical bearings with a friction coefficient of $\mu_e = 0.44\%$. This result would also suggest that the friction force on the lateral bearings is negligible.

The results shown in Figures 7(a) and (b) indicate that the dissipative forces obtained during the low-velocity tests (S1, S2, S3, T1, T2, T3) are somewhat larger than those calculated from the model. As shown in Figures 7(c) and (d), these differences can be accounted for by the additional term $12.04\mathrm{e}^{(-78.5|\dot{u}_x|)}$ kN for $\dot{u}_x$ in m/s. This term could represent a correction to the assumed $|\dot{u}_x|^{0.5}$ velocity dependence for low velocities, or a transition from static to dynamic friction coefficients.

Considering this correction, the dissipative force can be represented by

$$F_{\mathrm{D}}(t) = \mu_e F_z + C_e |\dot{u}_x|^{0.5} + a\mathrm{e}^{(-b|\dot{u}_x|)} \tag{22}$$

where $\mu_e = 0.44\%$, $C_e = 44.58\,\mathrm{kN/(m/s)}^{1/2}$, $a = 12.04\,\mathrm{kN}$ and $b = 78.5\,\mathrm{s/m}$. Figure 9 shows the decomposition of the total dissipative force (excluding the low-velocity correction) for the case of nominal hold-down nitrogen pressure ($F_z = 5783\,\mathrm{kN}$). In this case, the Coulomb friction force in the vertical bearings amounts to 26.0 kN, while the viscous component adds a dissipative force of 44.6 kN at a velocity of 1.0 m/s. The low-velocity correction term would add a force of 12.0 kN at zero velocity, but this term becomes negligibly small for velocities higher than 3 cm/s.

To verify the quality of the identified model of the dissipative forces, the identified and simulated total dissipative forces *vs* table displacement curves for tests S1 and S4 are compared in Figures 6(a) and (b). Also, Figures 6(c) and (d) show the corresponding identified and simulated total
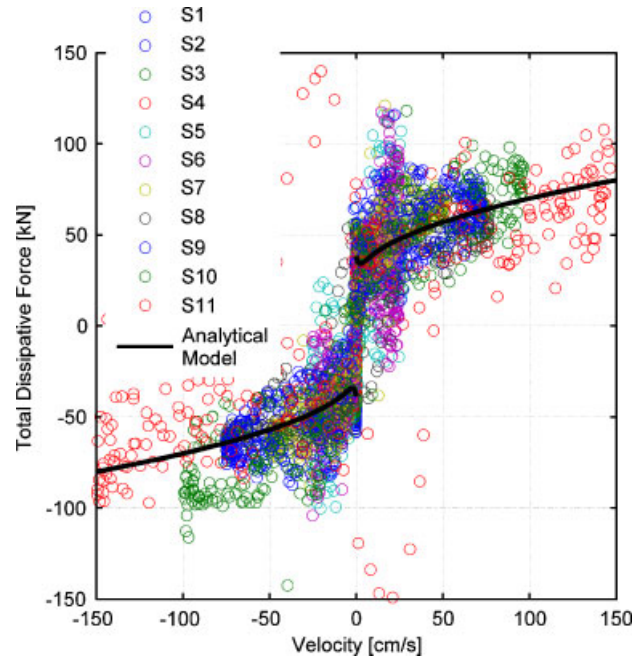
Figure 10. Scatter plot of instantaneous dissipative force *vs* instantaneous velocity for tests S1–S11 (13.8 MPa nitrogen pressure in the hold-down struts). Analytical model is shown as solid line.

dissipative force *vs* table velocity curves. It is apparent that the low-velocity correction term needs to be included for test S1 in which the peak velocity is only 1 cm/s.

A final comparison is presented in Figure 10 in which the scatter plot of instantaneous values of $F_D(t)$ *vs* $\dot{u}_x(t)$ for tests S1–S11 is shown together with the analytical model given by Equation (22). It is apparent from Figure 10 that the model fits the general trend of the data, and that the scatter is of the order of ± 20 kN. Clearly, it is difficult to isolate the dissipative forces from the inertial and elastic forces as the amplitudes of these forces are significantly larger. The dissipative forces are typically less than 0.08 MN (Test S10) while the inertial and elastic forces can be as large as 2.3 MN (Test S12) and 0.95 MN (Test T8), respectively.

3.5. Hysteresis loops for triangular tests

The previous discussion of the dissipative forces is based mostly on the results obtained during sinusoidal tests which involve platen displacements that do not exceed 20 cm. On the other hand, many of the triangular tests involve platen displacements that exceed 50 cm and velocities exceeding 50 cm/s. Because of the large volumes of oil involved (large swept displacements), these triangular tests are of short duration (3–12 s) and include only a few (2–3) cycles. Under these conditions, the hysteresis loops for triangular tests exhibit some features which are not clearly observable in the hysteresis loop for the sinusoidal tests.

Figure 11(a) and (b) show the hysteresis loops relating the instantaneous reduced force, $F_R(t) = F_A(t) - M_e \ddot{u}_x(t) - K_e u_x(t)$, and the corresponding recorded platen displacement $u_x(t)$ for tests
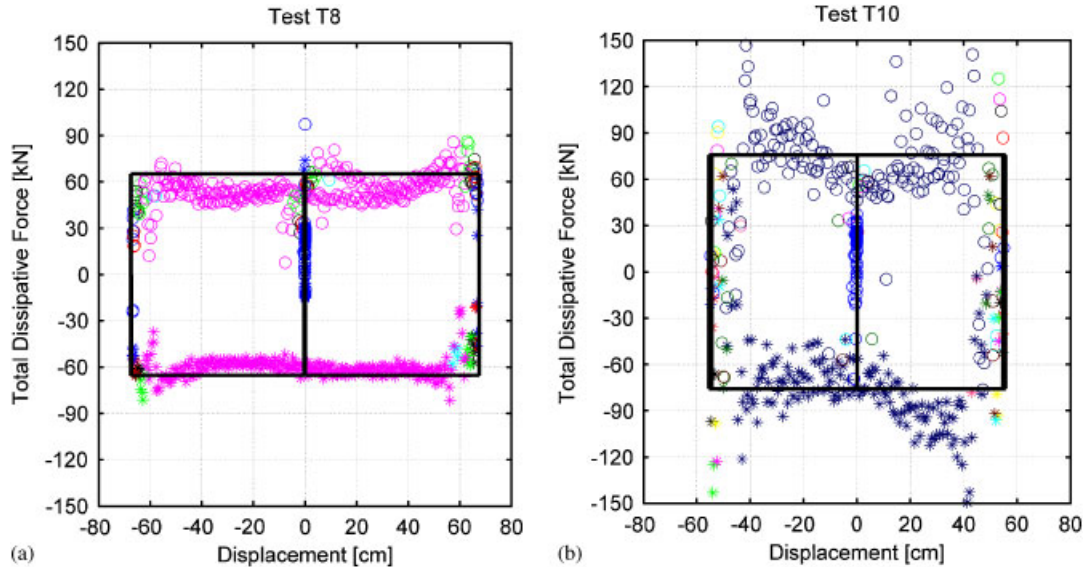
Figure 11. Instantaneous total dissipative forces *vs* instantaneous platen displacement for tests (a) T8, and (b) T10 (13.8 MPa nitrogen pressure in the hold-down struts). Analytical model is shown with solid lines.

T8 and T10. These tests are characterized by maximum platen velocities of 50 and 100 cm/s, respectively. The values of K_e listed in Table I ($K_e = 1.27$ MN/m for T8, and $K_e = 1.25$ MN/m for T10) were used in an attempt to have the reduced force $F_R(t)$ represent the total dissipative force $F_D(t)$ without contamination by the apparent changes of stiffness. A value of $M_e = 144$ ton was used in both cases. Also shown in Figures 11(a) and (b) are the values of $F_D(t)$ calculated by use of Equation (22) for the maximum velocity attained during each test. The results suggest that there is an additional nonlinear component of the dissipative force not included in Equation (22), which appears to increase with both instantaneous displacement and velocity. This additional dissipative force reaches a peak of 20–70 kN and appears to be significant only when the platen displacement exceeds 50 cm and the platen velocity exceeds 75 cm/s.

4. MODEL VALIDATION

The parameters of the NEES-UCSD LHPOST model identified in the previous section are based on the system response data for periodic sinusoidal and triangular excitations. It is important to verify that the resulting model is also capable of representing the more common shake table tests involving earthquake ground motions and white noise excitations. To verify the accuracy of the model, the total actuator force will be simulated by using

$$F_A(t) = M_e \ddot{u}_x(t) + K_e u_x(t) + (C_e |\dot{u}_x(t)|^\alpha + F_{\mu_e}) \, \text{sign}(\dot{u}_x(t)) \tag{23}$$
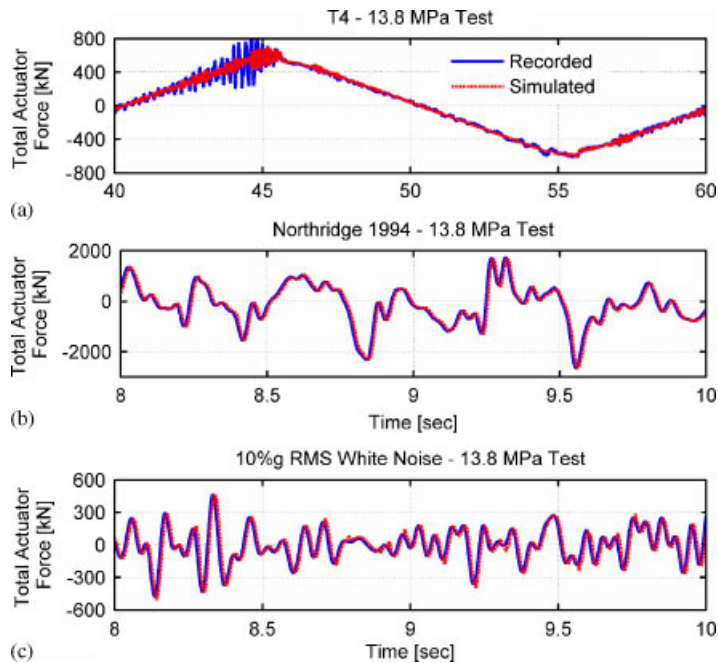
Figure 12. Comparisons of recorded and simulated total actuator forces for the following tests: (a) T4; (b) Northridge-1994 earthquake (100%); and (c) WN10%g (13.8 MPa nitrogen pressure in the hold-down struts).

and the results will be compared with the total actuator force recorded during various tests. Note that the simulations are based on the actual recorded displacement, velocity, and acceleration.

Comparisons of the recorded and simulated total actuator force time histories for three different tests are shown in Figure 12. The comparisons correspond to triangular test T4 ($u_{max} = 50$ cm, $\dot{u}_{max} = 10$ cm/s, $T = 20$ s), to an earthquake simulation test using the Northridge 1994 Cedar Hills Station ground motion with a peak acceleration of $1.81g$, and a white noise test with $0.10g$ root mean square acceleration (WN10%g). In order to see the details of the comparisons, only amplified segments of the time histories are shown. It is apparent from the results in Figure 12 and, from the rest of the time histories, that the model given by Equation (23), with the model parameters estimated previously, is capable of reproducing the recorded total actuator force for different types of tests.

An alternative type of verification consists of using the model to obtain the motion of the platen by integration of Equation (23) using the recorded total actuator force as input. The results of such an analysis for sinusoidal test SR9 ($u_{max} = 0.38$ m, $\dot{u}_{max} = 1.20$ m/s, $\ddot{u}_{max} = 0.384g$, $T = 2$ s) are shown in Figure 13. The recorded total actuator force was low-pass filtered with cut-off frequency of 0.6 Hz and Equation (23) was integrated numerically using the fixed-step Runge–Kutta method. The agreement between the recorded and simulated table velocity and displacement is excellent.
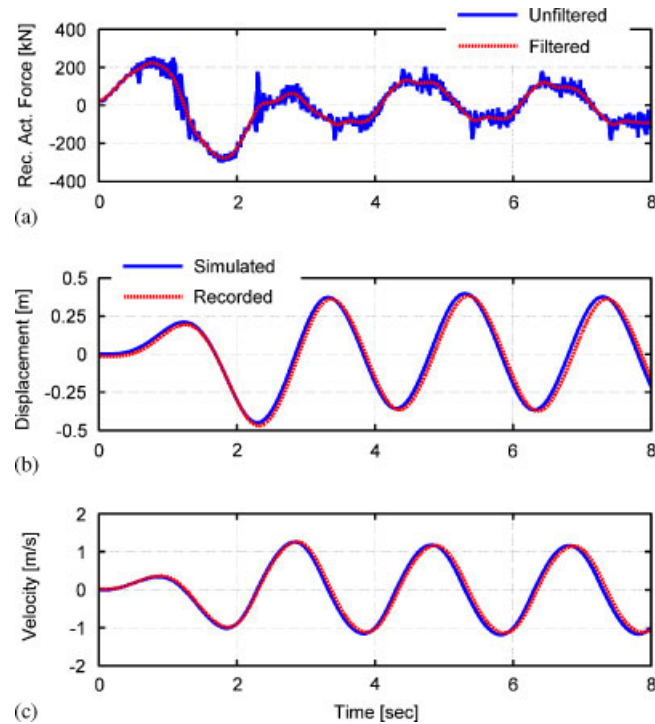
Figure 13. Comparison of recorded and simulated table velocity (c) and displacement (b) using as input the recorded total actuator force (a) for test SR9.

5. CONCLUSIONS

1. A mathematical model for the mechanical components of the NEES-UCSD LHPOST has been presented. It has been shown that several non-linear terms arising from the significant displacements and rotations of the hold-down struts are small, and that a simplified model including an effective horizontal mass, an effective horizontal stiffness due to the pre-charge pressure in the hold-down struts, and dissipative force terms composed of classical Coulomb friction and viscous damping elements is sufficient to simulate the response of the system.

2. The identification of the parameters of the mechanical sub-system of the NEES-UCSD LHPOST by using the experimental hysteresis loops leads to the following conclusions:

   (i) The experimental results indicate that the elastic restoring force acting on the platen is essentially provided by the pre-charge nitrogen pressure in the hold-down struts, the elastic force is essentially a linear function of the longitudinal displacement of the platen, and the effective horizontal stiffness corresponds to $K_e = 1.27\,\mathrm{MN/m}$ for the operational pressure of 13.8 MPa.

   (ii) The best estimate of the effective horizontal longitudinal mass of the table is $M_e = 144$ ton. This vertical mass includes the mass of the platen and of the cylinders of the two hold-down struts, and part of the mass of the two actuators. The experimental

data confirm that non-linear inertial terms are small within the range of table motions considered.

(iii) The analysis appears to show that the total dissipative force can be broken down into three main components: (i) Coulomb friction acting on the vertical bearings with a friction coefficient of 0.44%; (ii) a viscous force proportional to the square root of the velocity and with a damping constant of $44.6 \, \text{kN}/(\text{m/s})^{0.5}$; and (iii) a small force decreasing exponentially with the table velocity given by $12.04 e^{(-78.5|\dot{u}_x|)}$ kN for velocity in m/s. This last component may reflect a transition from static to dynamic friction and becomes negligibly small once the velocity has exceeded a threshold of say 5 cm/s. Additional dissipative forces, not fully identified, arise for large platen displacements (>50 cm) and velocities (>75 cm/s).

3. Although the parameters of the model considered herein have been identified by using the response during periodic sinusoidal and triangular excitations, it has been shown that the resulting model is also capable of representing the more common shake table tests involving earthquake ground motions and white noise excitations.

ACKNOWLEDGEMENTS

REFERENCES

1. Hwang JS, Chang KC, Lee GC. The system characteristics and performance of a shaking table. *NCEER Report No. 87-0004*, National Center for Earthquake Engineering Research, State University of New York at Buffalo, NY, 1987.
2. Rinawi AM, Clough RW. Shaking table–structure interaction. *EERC Report No. 91/13*, Earthquake Engineering Research Center, University of California at Berkeley, CA, 1991.
3. Clark A. Dynamic characteristics of large multiple degrees of freedom shaking tables. *Proceedings of the 10th World Conference on Earthquake Engineering*, Madrid, Spain, 1992; 2823–2828.
4. Conte JP, Trombetti TL. Linear dynamic modeling of a uni-axial servo-hydraulic shaking table system. *Earthquake Engineering and Structural Dynamics* 2000; **29**(9):1375–1404.
5. Williams DM, Williams MS, Blakeborough A. Numerical modeling of a servo-hydraulic testing system for structures. *Journal of Engineering Mechanics* (ASCE) 2001; **127**(8):816–827.
6. Shortreed JS, Seible F, Filiatrault A, Benzoni G. Characterization and testing of the Caltrans seismic response modification device test system. *Philosophical Transactions of the Royal Society of London Series A* 2001; **359**:1829–1850.
7. Crewe AJ, Severn RT. The European Collaborative Programme on evaluating the performance of shaking tables. *Philosophical Transactions of the Royal Society of London Series A* 2001; **359**:1671–1696.
8. Trombetti TL, Conte JP. Shaking table dynamics: results from a test analysis comparison study. *Journal of Earthquake Engineering* 2002; **6**(4):513–551.
9. Twitchell BS, Symans MD. Analytical modeling, system identification, and tracking performance of uniaxial seismic simulators. *Journal of Engineering Mechanics* (ASCE) 2003; **129**(12):1485–1488.
10. Thoen BK, Laplace PN. Offline tuning of shaking tables. *Proceedings of the 13th World Conference on Earthquake Engineering*, Paper No. 960. Vancouver, BC, Canada, 1–6 August 2004.
11. Van Den Einde L, Restrepo J, Conte JP, Luco E, Seible F, Filiatrault A, Clark A, Johnson A, Gram M, Kusner D, Thoen B. Development of the George E. Brown Jr. network for earthquake engineering simulation (NEES) large

high performance outdoor shake table at the University of California, San Diego. *Proceedings of the 13th World Conference on Earthquake Engineering*, Paper No. 3281. Vancouver, BC, Canada, 1–6 August 2004.
12. Website: http://nees.ucsd.edu/.
13. Bondonet G, Filiatrault A. Frictional response of PTFE sliding bearings at high frequencies. *Journal of Bridge Engineering* (ASCE) 1997; **2**(4):139–148.
14. Thoen BK. 469D Seismic Digital Control Software. MTS Corporation, 2004.
15. Kusner DA, Rood JD, Burton GW. Signal reproduction fidelity of servo-hydraulic testing equipment. *Proceedings of the 10th World Conference on Earthquake Engineering*, Rotterdam, 1992; 2683–2688.
16. Zhao J, Shield C, French C, Posbergh T. Nonlinear system modeling and velocity feedback compensation for effective force testing. *Journal of Engineering Mechanics* (ASCE) 2005; **131**(3):244–253.